Article

Programmable Parallel Optical Logic Gates on a Multimode Waveguide Engine

Tao Chen [1,2,†], Zhangqi Dang [1,2,†], Zhenming Ding [1,2] and Ziyang Zhang [2,*]

1   College of Information Science and Electronic Engineering, Zhejiang University, Hangzhou 310027, China
2   Laboratory of Photonic Integration, School of Engineering, Westlake University, Hangzhou 310024, China
*   Correspondence: zhangziyang@westlake.edu.cn
†   These authors contributed equally to this work.

Abstract: Optical logic gates have been proposed and demonstrated on a function programmable waveguide engine constructed using buried silicon nitride waveguides in polymer and a set of thermal electrodes. The device can perform logic AND or OR operations for the input signals *A* and *B*, each containing two bits of information, in parallel. The input signals, in the form of binary current values in the electronic domain, are applied to a subset of thermal electrodes, while the computed logic states are converted to optical intensity variations at the single-mode waveguide outputs. The rest of the electrodes work as weights to define the device function, either AND or OR, by adjusting the light interference in the multimode waveguide through thermo-optic effect. Simulations were first performed to reveal the nonlinear response of the received light intensity with respect to the applied current, thus allowing complex and effective manipulation of the light field on the waveguide engine. After chip fabrication and system integration, 65,536 experiments were performed automatically. The data are fed into a sorting program to find the valid settings that satisfy the respective truth table out of the 283,852,800 possible input/weight/output combinations. Four cases of operations for the AND and OR gates are presented in the end, with different bar and contrast values. This simple, low-cost yet powerful engine may be further developed for applications in on-chip photonic computing and signal switching.

Keywords: optical logic gate; silicon nitride; programmable photonics; multimode waveguide; thermo-optic effect

1. Introduction

Over the last few decades, the exponentially increasing demand for transmission capacity in optical fiber communication networks has led to the fast development of photonic integrated circuits (PICs) as an attractive and practical solution to expand capacity while keeping the cost low, compared to conventional solutions using the bulky assembly of discrete, free-space components [1,2]. Extra and often expensive procedures are needed to improve the stability and robustness of the free-space optical assembly to secure their applications in the daedal environment. The integration of optical components and functions into a large-scale PIC has shown clear advantages, as this technology keeps bringing new functionalities under reasonable power consumption and small footprint.

Beyond optical communication, PICs are expected to open up new ways to quench the ever-increasing thirst for computation power, raised by today's big data and artificial intelligence technology [3,4]. The key advantage is that photonic computation is carried out by light propagation that needs essentially no processing power and allows parallel treatment of massive data. It would enable applications that are unreachable by conventional electronic computing technology, those requiring low latency, high bandwidth, and low power-consumption, at the same time [5,6].

Under PIC-based photonic computation technology, it is believed by many that the property of photons makes it difficult to realize optical digital gates, whereas in the electronic domain the logic gates can be readily made by a series of transistors. Nevertheless, optical logic gates have been reported with different waveguide structures, such as active Mach-Zehnder interferometers (MZIs) [7,8], microring resonators (MRRs) [9], directional couplers (DCs) [10], multimode interference devices (MMIs) [11,12], QR code-like nanostructures [13], etc. Several material platforms, including silicon-on-insulator (SOI) [9], plasmas [14], lithium niobate [15], photonic crystals [16], nonlinear materials [17], etc., are dedicated to implementing the on-chip logic operation for signal process and photonic computing. Two methods are widely used in PIC-based logic devices [18]. The first method is based on the linear interference, where the input stays in the optical domain and the phases/amplitudes are taken to be the input logic states. This method is simple, convenient, and easy to implement with clear mechanics. However, it is still challenging to precisely control the phase difference between the various signals, though phase-shifted-keying [11] has matured over the years and been implemented in practical transmission networks. As the devices often require high structure/phase accuracy in the fabrication process, many designs have not been verified experimentally [10–15,17]. Furthermore, Ref. [19] adopts the input logic as the electrical pulse train (EPS), instead of the optical phase. The continuous wave (CW) light signal is used as the carrier only. Although this method avoids the accurate control of optical phases, the input EPS needs modulate the microring resonators precisely and the output information is read out at specific resonant wavelengths, thus requiring a complex and expensive system with broadband tunable laser and spectrum analyzing equipment.

The cascaded methods can effectively extend the number of operation logic bits for a large-scale computing network. However, they suffer from the often inefficient optical-electrical-optical (O/E/O) conversions [8]. The nonlinear optical effects can also be adopted to develop various kinds of complex logic devices. However, the nonlinear optical materials with large nonlinear susceptibility and ultrafast response are often expensive and require delicate processing.

In our previous works [20,21], we have demonstrated that the thermo-optic multimode waveguide is a powerful platform for programmable multi-functional PICs. The multimode interference (MMI) devices have shown desirable features, such as simple and compact structure, large bandwidth, low-loss, and good fabrication tolerance. The logic input can take the binary current values through the electrodes, while the input light can be continuous and works only as a carrier. Through a combination of thermo-optic and multimode interference effect, the output is converted into light intensity variations as defined in the truth table. However, the nonmonotonic response of the received light intensity with respect to the applied current makes it difficult to accurately predict the desirable logic functions. A current sweeping method can be introduced to search for the right configurations on the input and weight electrodes.

Recently, we have developed an optical computing/switching engine based on a multimode waveguide and a series of thermal electrodes to alter the light interference in the multimode region experimentally, actively, and automatically, until the desired pattern is reached at the output plane, so as to define the target function [21]. We name it function programmable waveguide engine (FPWE). With this technology, an optical NOT logic gate is demonstrated, capable of processing 4 bits of electronic logic signals in parallel. In this work, we explore further into the FPWE technology and present a function versatile logic gate capable of parallel two-bit operation for the logic AND or OR function, defined by refreshing/updating the electrode (input and weight) settings. Going further on from the previous work [21], the mechanism is investigated in detail, the data sorting algorithm is explained, and different levels of operations are explored for the target functions. We show that the proposed waveguide engine can even multiplex the logic AND and OR operations in parallel on the same chip with identical input, weight, and output. Only the bar values are set to be different for distinguishing the state of "0" and "1" for various logic operations.

In particular, we stress that the index tuning in the multimode region is a powerful method, as it can alter the total number of the guided eigenmodes, their individual modal profiles, as well as their propagation constants; while, in a single mode waveguide, the index tuning usually only varies the propagation constant, i.e., the phase of light passing through. We reveal that the thermal tuning process, similar to other E/O or O/E conversions, is essentially nonlinear, by drawing the curve relating the change of light intensity at a given output port to the electronic input in the form of current. This is fundamentally different to a conventional Mach-Zehnder interferometer (MZI) network, where the relation between the all-optical signals through the layers is considered as a linear transformation. This feature forms the foundation for the further development of the FPWE technology as an all-optical neutral network with built-in nonlinear activation function, but using only linear optical materials. This engine can be easily expanded, without cascades, to form a large-scale general hardware platform for the multi-bit logic operations and other versatile functions. We believe this work can inspire the development of programmable PICs for advanced communication and computing applications.

2. Engine Architecture and Working Mechanism

Figure 1a shows the architecture of the FPWE to be used as a logic gate. The input signal A and B, each containing two electrodes, i.e., two bits of logic information, are a subset of the electrode matrix E. The input logic signals stay in the electronic domain and take the form of current through the electrode, i.e., low current for logic "0" and high current for logic "1". The carrier light itself contains no information and the logic output C is evaluated from the optical intensities measured on a subset of the waveguide outputs O, as the result of the multimode interference.
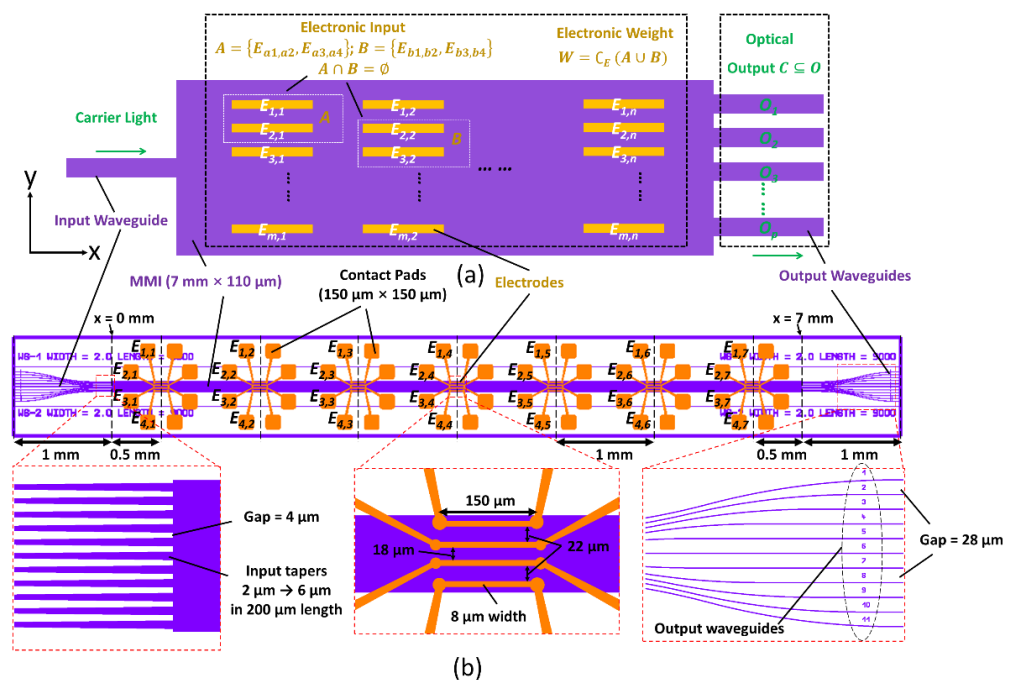
Figure 1. (**a**) Architecture of the function programmable waveguide engine (FPWE) to be used as a two-bit logic gate. The optical path contains an input waveguide, a multimode waveguide, and a series of output waveguides. Both the electronic inputs A, B, and the weights, can be chosen from the electrode network E. The logic outputs C are converted to optical intensity variations to be collected from two waveguide ports in O. (**b**) Actual chip design showing the layout of the electrode network. The redundant waveguide ports are reserved for further development. The insets are the detailed designs of the input tapers, electrodes, and the output waveguides.

The choice of electrodes forming A [$E_{a1, a2}$, $E_{a3, a4}$] and B [$E_{b1, b2}$, $E_{b3, b4}$] can be arbitrary based on the target functions. Figure 1a shows only one possible option for A and B, but the input electrodes are not necessarily chosen next to each other. A and B must be independent, i.e., "$A \cap B = \varnothing$". The rest of the electrodes in E are left as the weight matrix W. The current flowing through the weight electrodes can be adjusted in multiple levels, or in an analog manner, in order to search for the ideal settings that satisfy the target truth table for the logic AND or OR operation.

The actual chip design is displayed in Figure 1b. The size of the MMI is designed as 7 mm × 110 μm. The input and output waveguides are placed symmetrically to the MMI waveguide. It contains 11 input waveguides on the left side and any waveguide can be chosen as the carrier light injection port. All the input waveguides go through a taper structure to improve the coupling with multimode waveguide. The gaps between the input tapers are set to 4 μm. Two out of 11 output waveguides can be chosen as the optical output C. Output tapers are also added with a gap of 28 μm. A network of 4 × 7 thermal electrodes are placed on the multimode waveguide, each containing two pads (150 μm × 150 μm) for contact/bonding. The electrodes are labeled according to the row and column number. The gaps between each electrode column are set to be 1.0 mm along the propagation direction x. In each column, the 4 electrodes are designed with the size of 150 μm × 8 μm. The redundancy in the waveguide ports as well as in the electrode number leaves room for the development of different logic and switching devices using the same chip, but under different input/weight/output choices.

The cross-section of the multimode waveguide is shown in Figure 2a. We choose to work on silicon nitride (SiNx) waveguide in polymer for its relatively compact size, simple fabrication steps, high thermo-optic effect, and low thermal conductivity, as well as the intrinsic high waveguide birefringence that is essential for the development of polarization diversity devices, such as polarization-sensitive Bragg grating filters [22], polarization beam splitter [23], polarization rotator [24], etc. The thickness of SiNx layer is 150 nm and the refractive index is 1.949 at 1550 nm, measured by an ellipsometer. The single-mode input/output waveguides have a width of 2 μm, while the width of the multimode waveguide is 110 μm. The polymer cladding (ZPU12 series from ChemOptics, Daejeon, Korea) has an index of 1.45. The top and bottom cladding thickness is 6 μm and 15 μm, respectively. The design concept can well be applied to other material platforms (e.g., silicon photonics, InP, silica PLC, polymer waveguide, etc.) and the refractive index tuning methods can also vary (thermo-optic effect, electro-optic effect, charge carrier injection, etc.).

Thermal electrodes of 150 μm in length, 8 μm in width, and 100-nm in thickness (10 nm Ti and 90 nm Au) are placed symmetrically on the surface of the top cladding with respect to the SiNx core. A 2D thermal solver (LUMERICAL HEAT) is used to calculate the temperature gradient numerically, assuming the silicon substrate as a heatsink (25 °C). The local cross-sectional temperature distribution when 20 mA current goes through one of the electrodes ($E_{4,4}$) is shown in Figure 2b. The temperature distribution is translated to the change of the refractive index by the thermo-optic coefficient of the polymer cladding (-1.14×10^{-4}/°C) and the silicon nitride core (2.45×10^{-5}/°C). When a small heater power is applied, the index change is small, the gradient is smooth, and the extra scattering loss introduced by the electrodes can be neglected. However, the changed multimode interference under weakly applied heater power can still result in large power variations at the output waveguides, which constitute the logic-switching mechanism. In this work, we consider the TM modes only. As most of the light field for the guided modes resides in the cladding, the negative thermo-optic effect of the polymer material dominates [25]. The eigenmode profiles are calculated using the mode solver from LUMERICAL MODE.

For the unheated waveguide shown in Figure 2a, the structure supports 41 modes for the TM polarization, whereas for the heated condition shown in Figure 2b, the structure supports only 38 modes with much altered profiles. The results are compared in Figure 2c,d for the fundamental modes and the highest-order guided modes. Figure 2e

further compares the total light field in the XY plane for the unheated and heated cases, respectively, calculated using the bi-directional eigenmode expansion method. When an electrode is switched on, the change in the interference pattern is clearly visible. To quantify this change, a monitor is placed at the output waveguide O_3 to record the optical power passing through when a different current is applied to the electrode $E_{4,4}$, as an example. The curve is plotted in Figure 2f, demonstrating a nonmonotonic and nonlinear change of the optical power change in response to the electronic current applied.
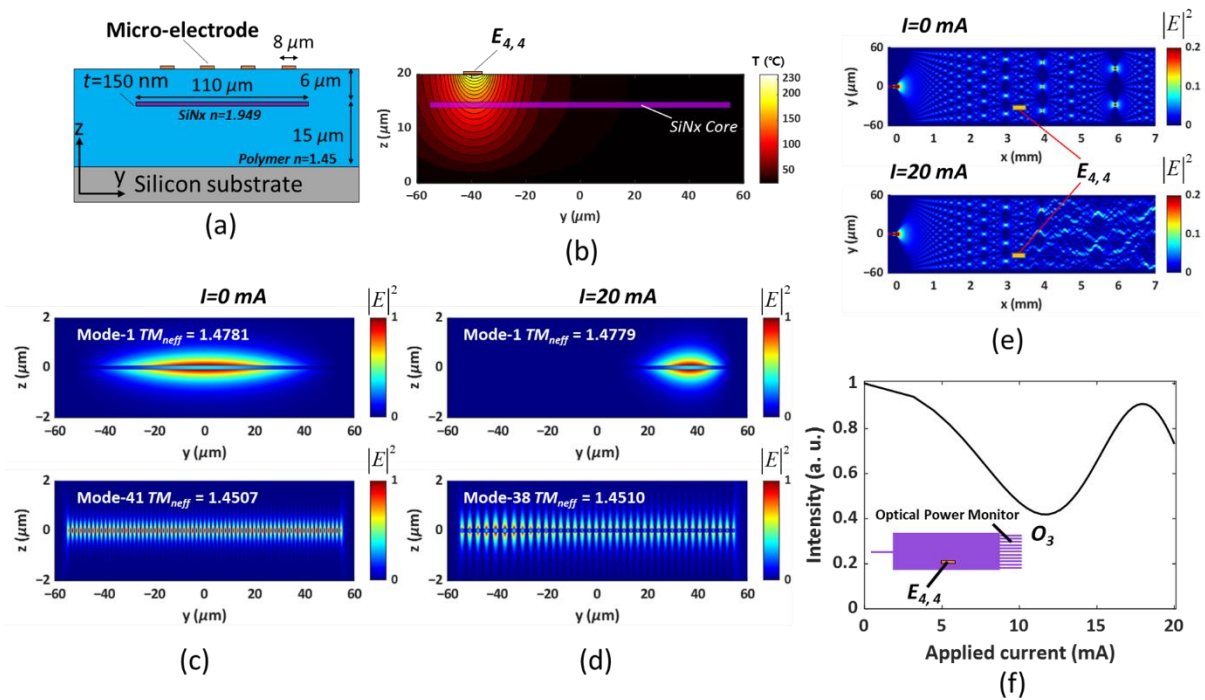
Figure 2. (**a**) Cross-section of the waveguide. (**b**) Temperature gradient by thermal simulation when 20 mA current is applied to the heater electrode $E_{4,4}$. (**c**,**d**) Comparison of the eigenmodes and (**e**) the corresponding multimode interference patterns with the heater ($E_{4,4}$) off and on. (**f**) Nonmonotonic and nonlinear relation between the current applied to $E_{4,4}$ and the intensity change at O_3 as a result of the complex electro-thermo-optic changes.

As it is difficult to conclude the response of the MMI waveguide by an analytical formula for any local refractive index change, the following empirical design rules are suggested when constructing a MMI-based logic gate. Firstly, the chosen multimode waveguide should support sufficient eigenmodes. The rule of thumb is to include at least 2 N modes, with N being the required output number. Once the waveguide thickness is set by the technology, the width can be varied to set the limit for higher order modes. Next, the multimode waveguide should be sufficiently long, so that the untuned MMI can at least reach the first 1 × N imaging point. However, the waveguide should not be much longer after the first 1 × 1 self-imaging point, as the MMI is intrinsically periodic. Extra length may facilitate interference tuning but would also result in an inefficient device. Finally, at least two columns of electrodes should be included, one column as the input and the other as weights. More weight electrodes would indeed allow for more complicated tuning of the MMI effect, but would also complicate the search process. One can leave some of the electrodes redundant, and only activate them if the search process fails.

The curve in Figure 2f comes as no surprise. From Ohm's law, the steady thermal power Q is related to the current by $Q = I^2 R$, where R is the resistance of the electrode, and I is the applied current. At steady state, the thermal power is related to the temperature change by the heat transport equation:

$$-\nabla\cdot(k\nabla T) = Q/V, \tag{1}$$

$$\nabla\cdot\boldsymbol{J} = 0, \tag{2}$$

where k is the thermal conductivity, ∇T is the temperature gradient, V is the volume, and $\boldsymbol{J}$ is the current density.

The heat transport equation can be solved numerically. The induced refractive index change Δn is related to the temperature change ΔT (before heating and upon heating at a steady state) by:

$$\Delta n = c_t \Delta T, \tag{3}$$

where c_t is the thermo-optic coefficient ($-1.14 \times 10^{-4}/^\circ$C) of the material and can be regarded as a constant within a reasonable temperature range. Under a given refractive index distribution, the eigenmodes can then be solved by Maxwell's equations. The total optical field at the output E_{tot} of a MMI waveguide can be given by:

$$E_{tot}(x,y,z) = \sum_{v=1}^{m} c_v \phi_v(y,z) e^{-j\beta_v x} \tag{4}$$

where x is the propagation direction and y,z is the profile which is perpendicular to the x direction. $\phi_v(y,z)$ is the eigenmode field, and β_v is their respective propagation constant. c_v is the coupling coefficient of the individual eigenmode numbered by v to the input light field, and m is the total number of the guided modes supported by the multimode waveguide [26]. The detected power P_o at one of the output ports x_o is proportional to the integral of the total intensity over the waveguide region:

$$P_o(x_o) \propto \iint |E_{tot}(x_o,y,z)|^2 dy dz \tag{5}$$

Through this chain of electrical–thermal–optical changes, one can expect a complicated, nonmonotonic function of P_o with respect to the applied current signal I. This function can be calculated numerically once the structure and material parameters are determined. The obtained curve in Figure 2f can also be fitted using a combination of analytical functions for a given current range. The significance is that it enables a nonlinear response of the output to the input when the input signals stay in the electronic domain and the output signals are taken as the corresponding light amplitude/intensity changes in the optical domain. We therefore expect that complex functions can be realized without resorting to nonlinear optical materials or other O/E/O conversions, e.g., in constructing deep neural networks for data sorting and image classification. In this work, however, we confine it to the function of logic gates only and leave AI-based applications for future development.

3. Chip Fabrication and System Integration

The fabrication follows the same process as described in [22]. Only standard contact lithography is used, and the chips are ready for measurement once the wafer is diced with a standard sawing machine without facet polishing.

Figure 3a shows the diagram of the FPWE system, and Figure 3b is a photo of the running system. For the O/E subassembly, an interconnected adapter is used to conduct the electronic signal from the main circuit board to the optical chip, but also as a sub-mount to hold the chip in place. The interconnected adapter allows secure fiber attachment and facilitates wire bonding to the pins. Considering that the electrode pads are only 100 nm thick without an extra plating step, a process is developed with the help of solder balls to ensure reliable bonding of the gold wires to the pads on the polymer cladding. A microscope photo is shown as the inset in Figure 3b. More details on the integration between the interconnected adapter and chip can be found in [21].

(a)

(b)
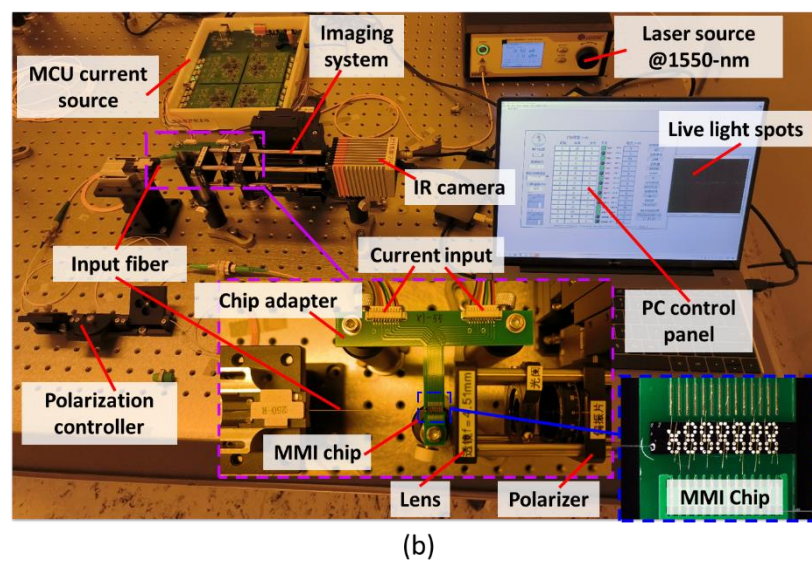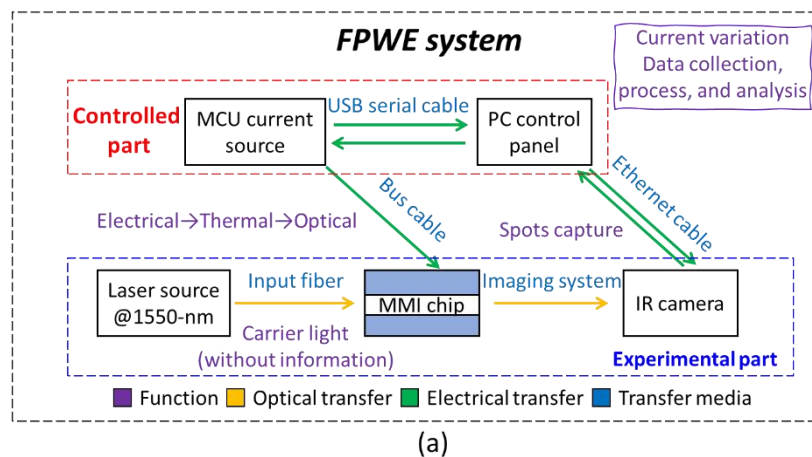
Figure 3. (**a**) Diagram and (**b**) actual photo of the FPWE system.

The main circuits board is based on the microcontroller unit (MCU), which has been custom-made from the advanced ARM-based 32-bit STM32F730XX series, capable of providing 16 current source channels. Each channel can adjust the current from 0 to 20 mA in the minimum adjusting step of 1 μA. All the 16 current channels are calibrated before use and the inaccuracy stays at the level of ±0.1%. The sub-mount/interposer is plug-connected to the MCU current source via two bus cables.

A continuous-wave laser at 1550-nm is adopted as the carrier light. Without high-speed PDs at hand, we have built an imaging system to capture the light from the open chip facet by an infrared (IR) camera. A polarizer is inserted into the imaging system to select only the TM light for analysis. After that, a central computer is used to update the current values in the MCU-based circuit board (via USB cable by Modbus protocol) and get the captured output from the IR camera (via ethernet cable by GigE vision protocol). The intensity variation of each output waveguide is then identified, saved, and processed in the central computer. The LabVIEW program provides the graphical user interface and synchronizes the MCU-based circuits board and camera. While the response time for the thermo-optic effect in polymer is on the millisecond scale, sufficient time should also be given for the image to stabilize (camera refresh rate is 100 Hz, and the image integration time is 100 ms). The thermo-optic response of the polymer material is on the millisecond scale [25]. In the experiment, each sweep process takes around 0.5 s considering the thermo-optic response, the photo capture of the CCD camera, and the data transmission

and storage. All these processes can be improved to sub-nanosecond scales with ultrafast electro-optic polymers [27], high-speed PDs and customized electronics.

As mentioned in our previous work [21], the experiment cycle of the FPWE system is reduced to 0.5 s, which is at least three orders of magnitude faster than the forward design using thermal and optical transmission simulations. This feature allows us to obtain a large amount of experimental data, sort them out using an automated program, and find the electrode settings that satisfy the target function, all experimentally. These settings may not be unique, and they are compared until the optimal values are found.

4. Data Acquisition, Analysis, and Discussion

To collect the data, we have developed a program to scan the electrode current values and store the camera shots automatically. We do not distinguish the input and weight electrodes at the data acquisition stage. At first, 8 electrodes [$E_{2,1}$ (22.0 Ω), $E_{1,2}$ (21.1 Ω), $E_{2,3}$ (22.6 Ω), $E_{1,4}$ (20.4 Ω), $E_{2,5}$ (21.3 Ω), $E_{1,6}$ (19.8 Ω), $E_{2,7}$ (21.1 Ω), $E_{4,7}$ (21.3 Ω)] are chosen, and the current can take 4 values [5 mA, 10 mA, 15 mA, 20 mA]. The total thermal power consumption ranges from 4.2 mW (5 mA is applied to all the 8 electrodes) to 67.8 mW (20 mA is applied to all the 8 electrodes). The rest of the electrodes remain off. In total, these combinations constitute 4^8 = 65,536 experiments, each resulting in an image of 523 kilobytes (PNG format, 640 × 512 pixels, 16-bit resolution). The scan process is complete within 9.1 h (0.5 s for each sweeping), storing around 32.6 gigabytes of data on the hard drive. After data collection, a program is developed to search for the target logic operations.

Among these data, 4 out of 8 electrodes need to be chosen as input A and B, as each input contains two bits, totaling A_8^4 = 1680 variations. It is noted that the sorting uses "permutation" rather than "combination", because the order between A (the first operation bits) and B (the second operation bits) and their respective high and low bits should all be distinguished as different configurations. For example, $A = [E_{2,1}, E_{1,2}]/B = [E_{2,3}, E_{1,4}]$ and $A = [E_{2,3}, E_{1,4}]/B = [E_{2,1}, E_{1,2}]$ are different configurations, though they use the same 4 electrodes. Two of the 4 applied current values need to denote the logic "0" (relatively low current) and "1" (relatively high current) state for all the logic bits in A and B (C_4^2 = 6). The other 4 electrodes remain as weights, which are fixed during the defined logic operations. Each of the weights can have one of the 4 current values, and the total number of the weight setting is calculated to be 4^4 = 256 for each specific input electrodes configuration. Two out of 11 waveguides should be chosen as the output C, adding up to A_{11}^2 = 110 options. Here, it also uses "permutation", not "combination", because the output values must be distinguished with high and low bits.

The sorting program must therefore process 1680 × 6 × 256 × 110 = 283,852,800 possible configurations. We name each combination as one setting. For each setting, the program must try 2^4 = 16 variations of the input states to compare with the target truth table for either logic AND or OR operation. A MATLAB program is developed to test the settings in parallel. Although the parallel computing toolbox of MATLAB is powerful, it is still time-consuming and may run out of memory if all 283,852,800 configurations are searched together. Therefore, we divided the data into 2 parts in the following search process. The first part is based on the input electrodes and their binary current values (1680 × 6). After that, the remaining configurations of the weights and their output ports (256 × 110) are individually implemented for each preprocessed configuration. If all the 16 input variations and their outputs satisfy the truth table, this setting, i.e., the specific combination of electrode selection, current choice, and waveguide outport selection, is recorded as a valid setting to define the device function.

The algorithm for data sorting is illustrated in Figure 4a, and the target truth tables are listed in Figure 4b. The criterion to judge the logic state of the optical output signal goes as follows. First, the optical power of a specific output channel is evaluated by adding up the relative pixel counts in the area where the output waveguide is imaged (20 × 20 pixels). For each of the 283,852,800 settings, an experimental truth table is generated using the optical power of the chosen waveguide ports and in the sequence as listed in Figure 4b. In

the experimental truth table, the high input current is taken as the logic "1" and the low input current is the logic "0". It is important to find a "bar" value that can judge the output lights as logical states to satisfy the target truth table. If the bar does not exist, this setting is invalid.
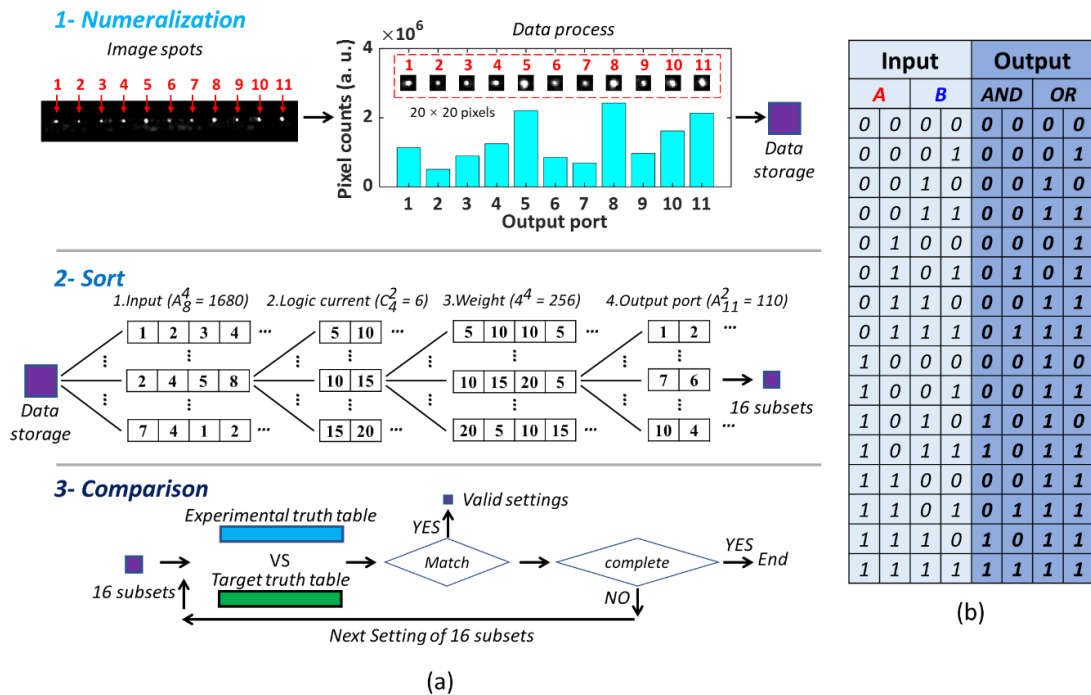
Figure 4. (**a**) Data sorting algorithm to find the valid settings that match the truth table. (**b**) The target truth table for the two-bit AND and OR logic operation.

Input				Output			
A		*B*		AND		OR	
0	0	0	0	0	0	0	0
0	0	0	1	0	0	0	1
0	0	1	0	0	0	1	0
0	0	1	1	0	0	1	1
0	1	0	0	0	0	0	1
0	1	0	1	0	1	0	1
0	1	1	0	0	0	1	1
0	1	1	1	0	1	1	1
1	0	0	0	0	0	1	0
1	0	0	1	0	0	1	1
1	0	1	0	1	0	1	0
1	0	1	1	1	0	1	1
1	1	0	0	0	0	1	1
1	1	0	1	0	1	1	1
1	1	1	0	1	0	1	1
1	1	1	1	1	1	1	1

(b)

A simple method to find the valid bar value is shown in the following. We first find the largest value of all the 16 cases for the locations where "0" output states (from the target truth table) should be and name it $C_{0\text{-}max}$. Then, we find the lowest value for the locations where "1" output states (from the target truth table) should be and name it $C_{1\text{-}min}$. We define **Contrast** = $C_{1\text{-}min} - C_{0\text{-}max}$. If **Contrast** > 0, we consider the experimental truth table agrees with the target truth table, and the setting is valid because all the states which should be "1" have larger optical power than the states which should be "0". Hence, a valid bar can be set to distinguish the "0" and "1" output states. We define the valid bar as $bar = (C_{0\text{-}max} + C_{1\text{-}min})/2$. Note that the bar can be different among the valid settings and also for the AND and OR gates. Nevertheless, we stick to this criterion, because once the setting is determined, the device function is defined with a fixed bar to judge the output states.

The evaluation of the optical power by camera counts is only an intermediate solution, and the chip can be integrated with high-speed PDs and subsequent electronics for a compact FPWE system in the future. The MATLAB program runs on a computer (Intel Core Xeon E-2286G CPU, 64G RAM, Windows 10 system) for 4 h until all the valid settings are found. As further work, fixed electronic inputs and fewer input/output waveguides can make the device more compact and improve the search efficiency. More efficient data sorting techniques will also be developed.

During the search for the valid settings, we follow a few steps, based on the choices of input electrodes, weight electrodes, and output waveguide ports. First, we allow the selection of input electrodes, weight electrodes, and output ports to be independent for the logic AND and OR gates, as a general case **S-I**. In this case, the AND and OR logic operations can both be realized on the same chip, but the input, weight, and output need to be changed to switch the logic functions.

Next, for all the valid settings that satisfy **S-I**, we set the extra rule that the input electrodes must be the same for both the AND and OR gates, as case **S-II**. In this case, the input is fixed, the functions can be switched with different settings of weight and output.

Under **S-II**, we further confine that the output waveguide ports must also be the same, as case **S-III**. This is convenient in practice as both the input and the output ports are fixed. The weight electrodes and output bar need to be changed when the chip switches its function between AND and OR gates.

Finally, we also find that under **S-III**, even the weight settings can be the same; i.e., there exist some solutions in which the selection of input electrodes and output ports, plus the current values on the weight electrodes, can all stay the same, as case **S-IV**. The device is either AND or OR gate, depending only on the choices of ***bar***.

Table 1 summarizes the total number of valid settings under these 4 cases along with their conditions with arbitrary ($\forall$) or same (=) parameters. It is noted that some combinations are not discussed in Table 1. That is because the input electrodes are commonly fixed for practical use. The weights can be changed for the function switching and the output ports can be different to guide the results into various receivers.

Table 1. The number of valid settings under **S-I** to **S-IV** case.

Case	A, B (Input)	W (Weight)	C (Output)	Valid Settings	
				AND	OR
S-I	Arbitrary ($\forall$)	Arbitrary ($\forall$)	Arbitrary ($\forall$)	17,184	15,168
S-II	Same (=)	Arbitrary ($\forall$)	Arbitrary ($\forall$)	12,912	12,552
S-III	Same (=)	Arbitrary ($\forall$)	Same (=)	5592	5496
S-IV	Same (=)	Same (=)	Same (=)	2320	

S-IV $\subseteq$ **S-III** $\subseteq$ **S-II** $\subseteq$ **S-I**, the symbols of arbitrary and same settings are in the brackets.

For **S-I**, the device can provide the highest contrast between $C_{0\text{-}max}$ and $C_{1\text{-}min}$. Table 2 summarizes one of these settings with the screenshot of the light spots for each item in the truth table. The values are normalized with the maximal single pixel count given by the chosen camera in the image area. For **S-III**, the contrast is low compared to **S-I**, and one of the settings is summarized in Table 3. For the extreme case **S-IV**, the bar is changed both for logic operations and output ports. One of these settings is summarized in Table 4.

A comparison between this work and previous works is worth discussing. Different from phase-controlled methods, the input logic is replaced by the electric signal based on the applied current of the electrode. Our design eliminates the need for precise phase tuning. Instead, the local refractive index change in the multimode waveguide effectively renders largely different interference patterns at the output. We believe this method provides a general system and can be widely compatible with various material platforms and refractive index tuning mechanics. Nonlinear materials are indeed attractive as they can be used to construct various logic gates with ultrafast response, but the demand on high input power and often expensive fabrication technology may limit their implementation in practice.

The current FPWE system still faces several challenges. For system integration, fast photodiodes should be attached to the output waveguides instead of the camera shot. The processing electronics and circuit boards should all be high-speed compatible. On the fundamental level, the prediction of the multimode interference is complex and difficult. Although the time-consuming electromagnetic simulations are avoided by direct experimental sweeping, the search process afterwards is still tedious and may take several hours. To solve this problem, the MMI can be modeled by an equivalent AI-based neural network, with which the realizable functions can be predicted and pre-programed. This would greatly improve the efficiency of specific functional programming. In this work, a large MMI chip with redundant waveguide ports and electrode numbers is adopted for simple logic operations. The underlying guidelines to map the device size, e.g., the MMI dimensions and number of supported modes, to the specific functions, need to be further

explored. More compact, efficient, and scalable devices with precise thermal configurations can then be designed systematically.

Table 2. AND and OR gate settings of **S-I**. [Input-∀, Weight-∀, Output-∀].

S-I: AND								S-I: OR							
Weight: $E_{1,2}$ = 10 mA, $E_{2,3}$ = 10 mA, $E_{1,6}$ = 15 mA, $E_{2,7}$ = 20 mA								Weight: $E_{2,1}$ = 20 mA, $E_{2,5}$ = 20 mA, $E_{1,6}$ = 20 mA, $E_{4,7}$ = 5 mA							
Input				Output		Screenshot		Input				Output		Screenshot	
A		*B*		O_3	O_9	O_3	O_9	*A*		*B*		O_5	O_8	O_5	O_8
$E_{1,4}$	$E_{2,5}$	$E_{4,7}$	$E_{2,1}$					$E_{1,4}$	$E_{1,2}$	$E_{2,3}$	$E_{2,7}$				
0	**0**	**0**	**0**	**0**(5.6)	**0**(5.0)			**0**	**0**	**0**	**0**	**0**(10.1)	**0**(5.0)		
0	**0**	**0**	**1**	**0**(14.2)	**0**(1.9)			**0**	**0**	**0**	**1**	**0**(13.4)	**1**(15.2)		
0	**0**	**1**	**0**	**0**(11.5)	**0**(2.8)			**0**	**0**	**1**	**0**	**1**(31.6)	**0**(7.3)		
0	**0**	**1**	**1**	**0**(22.6)	**0**(3.5)			**0**	**0**	**1**	**1**	**1**(35.6)	**1**(18.0)		
0	**1**	**0**	**0**	**0**(11.9)	**0**(2.8)			**0**	**1**	**0**	**0**	**0**(8.6)	**1**(45.9)		
0	**1**	**0**	**1**	**0**(10.6)	**1**(26.8)			**0**	**1**	**0**	**1**	**0**(9.8)	**1**(43.3)		
0	**1**	**1**	**0**	**0**(11.1)	**0**(3.6)			**0**	**1**	**1**	**0**	**1**(41.5)	**1**(30.0)		
0	**1**	**1**	**1**	**0**(20.8)	**1**(22.3)			**0**	**1**	**1**	**1**	**1**(29.0)	**1**(30.7)		
1	**0**	**0**	**0**	**0**(24.4)	**0**(5.8)			**1**	**0**	**0**	**0**	**1**(24.4)	**0**(6.4)		
1	**0**	**0**	**1**	**0**(26.2)	**0**(2.4)			**1**	**0**	**0**	**1**	**1**(25.7)	**1**(19.3)		
1	**0**	**1**	**0**	**1**(40.8)	**0**(4.1)			**1**	**0**	**1**	**0**	**1**(31.9)	**0**(5.9)		
1	**0**	**1**	**1**	**1**(44.2)	**0**(2.9)			**1**	**0**	**1**	**1**	**1**(31.9)	**1**(21.0)		
1	**1**	**0**	**0**	**0**(16.5)	**0**(5.1)			**1**	**1**	**0**	**0**	**1**(35.5)	**1**(53.0)		
1	**1**	**0**	**1**	**0**(26.7)	**1**(17.8)			**1**	**1**	**0**	**1**	**1**(26.0)	**1**(51.6)		
1	**1**	**1**	**0**	**1**(37.8)	**0**(3.8)			**1**	**1**	**1**	**0**	**1**(49.6)	**1**(25.8)		
1	**1**	**1**	**1**	**1**(38.9)	**1**(16.2)			**1**	**1**	**1**	**1**	**1**(31.5)	**1**(21.1)		
Input State: "0" = 15 mA; "1" = 20 mA				Output *bar* 1 = 32.2; *Contrast* 1 = 11.1 Output *bar* 2 = 11.1; *Contrast* 2 = 10.4				Input State: "0" = 5 mA; "1" = 15 mA				Output *bar* 1 = 18.9; *Contrast* 1 = 11.0 Output *bar* 2 = 11.2; *Contrast* 2 = 7.9			

Table 3. AND and OR gate settings of **S-III**. [**Input- = , Weight-∀, Output- = **].

S-III: AND									S-III: OR								
Weight: $E_{2,3}$ = 15 mA, $E_{1,4}$ = 10 mA, $E_{2,5}$ = 5 mA, $E_{4,7}$ = 15 mA									Weight: $E_{2,3}$ = 15 mA, $E_{1,4}$ = 15 mA, $E_{2,5}$ = 5 mA, $E_{4,7}$ = 15 mA								
Input				Output		Screenshot			Input				Output		Screenshot		
A		B		O_6	O_9	O_6	O_9		A		B		O_6	O_9	O_6	O_9	
$E_{1,2}$	$E_{2,1}$	$E_{1,6}$	$E_{2,7}$						$E_{1,2}$	$E_{2,1}$	$E_{1,6}$	$E_{2,7}$					
0	**0**	**0**	**0**	**0**(46.6)	**0**(24.3)				**0**	**0**	**0**	**0**	**0**(44.2)	**0**(18.8)			
0	**0**	**0**	**1**	**0**(41.3)	**0**(35.4)				**0**	**0**	**0**	**1**	**0**(41.4)	**1**(26.0)			
0	**0**	**1**	**0**	**0**(57.0)	**0**(23.3)				**0**	**0**	**1**	**0**	**1**(53.2)	**0**(15.6)			
0	**0**	**1**	**1**	**0**(55.5)	**0**(32.4)				**0**	**0**	**1**	**1**	**1**(51.8)	**1**(22.9)			
0	**1**	**0**	**0**	**0**(45.2)	**0**(30.6)				**0**	**1**	**0**	**0**	**0**(44.9)	**1**(26.9)			
0	**1**	**0**	**1**	**0**(45.2)	**1**(40.7)				**0**	**1**	**0**	**1**	**0**(43.7)	**1**(34.9)			
0	**1**	**1**	**0**	**0**(55.9)	**0**(30.0)				**0**	**1**	**1**	**0**	**1**(51.4)	**1**(26.3)			
0	**1**	**1**	**1**	**0**(55.7)	**1**(39.3)				**0**	**1**	**1**	**1**	**1**(49.8)	**1**(33.6)			
1	**0**	**0**	**0**	**0**(53.5)	**0**(20.0)				**1**	**0**	**0**	**0**	**1**(53.7)	**0**(13.7)			
1	**0**	**0**	**1**	**0**(49.7)	**0**(31.3)				**1**	**0**	**0**	**1**	**1**(49.6)	**1**(22.4)			
1	**0**	**1**	**0**	**1**(62.5)	**0**(19.7)				**1**	**0**	**1**	**0**	**1**(56.9)	**0**(13.2)			
1	**0**	**1**	**1**	**1**(59.9)	**0**(29.4)				**1**	**0**	**1**	**1**	**1**(54.3)	**1**(23.2)			
1	**1**	**0**	**0**	**0**(55.7)	**0**(30.7)				**1**	**1**	**0**	**0**	**1**(53.4)	**1**(26.8)			
1	**1**	**0**	**1**	**0**(52.0)	**1**(42.1)				**1**	**1**	**0**	**1**	**1**(50.2)	**1**(36.2)			
1	**1**	**1**	**0**	**1**(61.9)	**0**(32.0)				**1**	**1**	**1**	**0**	**1**(55.6)	**1**(28.3)			
1	**1**	**1**	**1**	**1**(59.9)	**1**(41.1)				**1**	**1**	**1**	**1**	**1**(55.4)	**1**(36.3)			
Input State: "0" = 5 mA; "1" = 10 mA				Output *bar* 1 = 58.4; *Contrast* 1 = 2.9 Output *bar* 2 = 37.4 *Contrast* 2 = 3.9					Input State: "0" = 5 mA; "1" = 10 mA				Output *bar* 1 = 45.6; *Contrast* 1 = 4.7 Output *bar* 2 = 22.3; *Contrast* 2 = 3.6				

Table 4. AND and OR gate settings of S-IV. **[Input- = , Weight- = , Output- =].**

S-IV: AND/OR							
Weight: $E_{2,3}$ = 15 mA, $E_{1,4}$ = 10 mA, $E_{2,5}$ = 5 mA, $E_{4,7}$ = 15 mA							
Input				Output		Screenshot	
A		B		O_6	O_9	O_6	O_9
$E_{1,2}$	$E_{2,7}$	$E_{1,6}$	$E_{2,1}$	AND/OR	ANR/OR		
0	0	0	0	0/0(46.6)	0/0(24.3)		
0	0	0	1	0/0(45.2)	0/1(30.6)		
0	0	1	0	0/1(57.0)	0/0(23.3)		
0	0	1	1	0/1(55.9)	0/1(30.0)		
0	1	0	0	0/0(41.3)	0/1(35.4)		
0	1	0	1	0/0(45.2)	1/1(40.7)		
0	1	1	0	0/1(55.5)	0/1(32.4)		
0	1	1	1	0/1(55.7)	1/1(39.3)		
1	0	0	0	0/1(53.5)	0/0(20.0)		
1	0	0	1	0/1(55.7)	0/1(30.7)		
1	0	1	0	1/1(62.5)	0/0(19.7)		
1	0	1	1	1/1(61.9)	0/1(32.0)		
1	1	0	0	0/1(49.7)	0/1(31.3)		
1	1	0	1	0/1(52.0)	1/1(42.1)		
1	1	1	0	1/1(59.9)	0/1(29.4)		
1	1	1	1	1/1(59.9)	1/1(41.1)		
Input State: "0" = 5 mA; "1" = 10 mA				**AND:** Output *bar* 1 = 58.4; *Contrast* 1 = 2.9 Output *bar* 2 = 37.4; *Contrast* 2 = 3.9			
				OR: Output *bar* 1 = 48.2; *Contrast* 1 = 3.1 Output *bar* 2 = 26.8; *Contrast* 2 = 5.1			

5. Conclusions

To summarize, a parallel two-bit logic gate is proposed using the FPWE technology. The mechanism is explained in theory and the nonlinear response of the light intensity variation (output) to the electronic input (in terms of current) is revealed. One experiment takes about 0.5 s, and in total 9.1 h are sufficient to complete the parameter sweep of 65,536 experiments and store the data. The process is about three orders of magnitude faster than the traditional, forward-design approach using thermal and optical simulations. This method also avoids the deviation between simulation and experiment altogether.

After data collection, a program and search criteria are defined to find the valid settings on the electrode network for the logic function out of the total 283,852,800 possible combinations. By the preliminary search for the valid settings of 8 electrodes with 4 applied current values (5 mA, 10 mA, 15 mA, 20 mA), a large number of logic AND or OR gates

can be realized independently (case **S-I**). Extra sort conditions are added to find the subset of valid settings for the same inputs (**S-II**), further for the same outputs (**S-III**), and finally also for the same weights but with different output bars (**S-IV**). The final settings under Case **S-IV** allow the selection of input electrodes and output ports, plus the current values on the weight electrodes, all to be the same. The device works either as an AND gate or an OR gate, depending solely on the choice of the *bar*.

With this work, we have further explored the power of the FPWE technology. For further development, a real-time search algorithm with a feedback mechanism or a trained neural network model can be induced to reach the target function more efficiently. Furthermore, an equivalent trained neural network model can be established to represent the response of the MMI waveguide. The input and the target output of a specific logic operation can be calculated, instead of searching all the experimental results. The neural network is then used to predict the remaining weight configuration to satisfy the target truth table. Development of the FPWE technology for advanced AI applications will be carried out in the next step. We believe the reported technology can inspire some new ideas in developing large-scale parallel optical logic gates and switching networks for advanced photonic applications.

Author Contributions: Conceptualization, Z.Z. and T.C.; methodology, T.C., Z.D. (Zhangqi Dang) and Z.Z.; software, T.C.; validation, T.C., Z.D. (Zhangqi Dang) and Z.D. (Zhenming Ding); formal analysis, T.C., Z.D. (Zhangqi Dang) and Z.Z.; investigation, T.C. and Z.D. (Zhangqi Dang); resources, Z.Z.; data curation, T.C.; writing—original draft preparation, T.C. and Z.D. (Zhangqi Dang); writing—review and editing, T.C. and Z.Z.; visualization, T.C.; supervision, Z.Z.; project administration, Z.Z. All authors have read and agreed to the published version of the manuscript.

Institutional Review Board Statement: Not applicable.

Informed Consent Statement: Not applicable.

Data Availability Statement: The data presented in this study are available from the corresponding author upon reasonable request.

Conflicts of Interest: The authors declare no conflict of interest.

References

1. Heck, M.J.; Bauters, J.F.; Davenport, M.L.; Doylend, J.K.; Jain, S.; Kurczveil, G.; Srinivasan, S.; Tang, Y.; Bowers, J.E. Hybrid silicon photonic integrated circuit technology. *IEEE J. Sel. Top. Quantum Electron.* **2012**, *19*, 6100117. [CrossRef]
2. Kish, F.; Lal, V.; Evans, P.; Corzine, S.W.; Ziari, M.; Butrie, T.; Reffle, M.; Tsai, H.-S.; Dentai, A.; Pleumeekers, J. System-on-chip photonic integrated circuits. *IEEE J. Sel. Top. Quantum Electron.* **2017**, *24*, 1–20. [CrossRef]
3. Li, C.; Zhang, X.; Li, J.; Fang, T.; Dong, X. The challenges of modern computing and new opportunities for optics. *PhotoniX* **2021**, *2*, 20.
4. Peng, H.-T.; Nahmias, M.A.; De Lima, T.F.; Tait, A.N.; Shastri, B.J. Neuromorphic photonic integrated circuits. *IEEE J. Sel. Top. Quantum Electron.* **2018**, *24*, 1–15. [CrossRef]
5. Wang, N.; Yan, W.; Qu, Y.; Ma, S.; Li, S.Z.; Qiu, M. Intelligent designs in nanophotonics: From optimization towards inverse creation. *PhotoniX* **2021**, *2*, 22. [CrossRef]
6. Shastri, B.J.; Tait, A.N.; Ferreira de Lima, T.; Pernice, W.H.; Bhaskaran, H.; Wright, C.D.; Prucnal, P.R. Photonics for artificial intelligence and neuromorphic computing. *Nat. Photon.* **2021**, *15*, 102–114. [CrossRef]
7. Kim, J.-Y.; Kang, J.-M.; Kim, T.-Y.; Han, S.-K. All-optical multiple logic gates with XOR, NOR, OR, and NAND functions using parallel SOA-MZI structures: Theory and experiment. *J. Lightwave Technol.* **2006**, *24*, 3392.
8. Kumar, S.; Bisht, A.; Singh, G.; Amphawan, A. Implementation of 2-bit multiplier based on electro-optic effect in Mach–Zehnder interferometers. *Opt. Quantum Electron.* **2015**, *47*, 3667–3688. [CrossRef]
9. Xu, Q.; Lipson, M. All-optical logic based on silicon micro-ring resonators. *Opt. Express* **2007**, *15*, 924–929. [CrossRef]
10. Fraga, W.; Menezes, J.; Da Silva, M.; Sobrinho, C.; Sombra, A. All optical logic gates based on an asymmetric nonlinear directional coupler. *Opt. Commun.* **2006**, *262*, 32–37. [CrossRef]
11. Ishizaka, Y.; Kawaguchi, Y.; Saitoh, K.; Koshiba, M. Design of optical XOR, XNOR, NAND, and OR logic gates based on multi-mode interference waveguides for binary-phase-shift-keyed signal. *J. Lightwave Technol.* **2011**, *29*, 2836–2846. [CrossRef]
12. Mohammadnejad, S.; Chaykandi, Z.F.; Bahrami, A. MMI-based simultaneous all-optical XOR–NAND–OR and XNOR–NOT multilogic gate for phase-based signals. *IEEE J. Quantum Electron.* **2014**, *50*, 1–5. [CrossRef]

13. Lu, Q.; Yan, X.; Wei, W.; Zhang, X.; Zhang, M.; Zheng, J.; Li, B.; Lin, Q.; Ren, X. High-speed ultra-compact all-optical NOT and AND logic gates designed by a multi-objective particle swarm optimized method. *Opt. Laser Technol.* **2019**, *116*, 322–327. [CrossRef]
14. Kumar, S.; Singh, L.; Chen, N.-K. Design of all-optical universal gates using plasmonics Mach-Zehnder interferometer for WDM applications. *Plasmonics* **2018**, *13*, 1277–1286. [CrossRef]
15. Kumar, S.; Raghuwanshi, S.K. Design of optical reversible logic gates using electro-optic effect of lithium niobate based Mach–Zehnder interferometers. *Appl. Opt.* **2016**, *55*, 5693–5701. [CrossRef] [PubMed]
16. Hussein, H.M.; Ali, T.A.; Rafat, N.H. A review on the techniques for building all-optical photonic crystal logic gates. *Opt. Laser Technol.* **2018**, *106*, 385–397. [CrossRef]
17. Nozhat, N.; Granpayeh, N. All-optical logic gates based on nonlinear plasmonic ring resonators. *Appl. Opt.* **2015**, *54*, 7944–7948. [CrossRef]
18. Minzioni, P.; Lacava, C.; Tanabe, T.; Dong, J.; Hu, X.; Csaba, G.; Porod, W.; Singh, G.; Willner, A.E.; Almaiman, A. Roadmap on all-optical processing. *J. Opt.* **2019**, *21*, 063001. [CrossRef]
19. Zhang, L.; Ji, R.; Jia, L.; Yang, L.; Zhou, P.; Tian, Y.; Chen, P.; Lu, Y.; Jiang, Z.; Liu, Y. Demonstration of directed XOR/XNOR logic gates using two cascaded microring resonators. *Opt. Lett.* **2010**, *35*, 1620–1622. [CrossRef]
20. Dang, Z.; Chen, T.; Ding, Z.; Liu, Z.; Zhang, X.; Jiang, X.; Zhang, Z. Multiport all-logic optical switch based on thermally altered light paths in a multimode waveguide. *Opt. Lett.* **2021**, *46*, 3025–3028. [CrossRef]
21. Chen, T.; Dang, Z.; Ding, Z.; Liu, Z.; Zhang, Z. Multibit NOT logic gate enabled by a function programmable optical waveguide. *Opt. Lett.* **2022**, *47*, 3519–3522. [CrossRef] [PubMed]
22. Zhang, Z.; Liu, D.; de Felipe, D.; Liu, A.; Keil, N.; Grote, N. Polymer embedded silicon nitride thermally tunable Bragg grating filters. *Appl. Phys. Lett.* **2013**, *102*, 181105. [CrossRef]
23. Sun, X.; Alam, M.; Aitchison, J.; Mojahedi, M. Compact and broadband polarization beam splitter based on a silicon nitride augmented low-index guiding structure. *Opt. Lett.* **2016**, *41*, 163–166. [CrossRef]
24. Sun, X.; Alam, M.; Aitchison, J.S.; Mojahedi, M. Polarization rotator based on augmented low-index-guiding waveguide on silicon nitride/silicon-on-insulator platform. *Opt. Lett.* **2016**, *41*, 3229–3232. [CrossRef] [PubMed]
25. Zhang, Z.; Keil, N. Thermo-optic devices on polymer platform. *Opt. Commun.* **2016**, *362*, 101–114. [CrossRef]
26. Soldano, L.B.; Pennings, E.C. Optical multi-mode interference devices based on self-imaging: Principles and applications. *J. Lightwave Technol.* **1995**, *13*, 615–627. [CrossRef]
27. Ullah, F.; Deng, N.; Qiu, F. Recent progress in electro-optic polymer for ultra-fast communication. *PhotoniX* **2021**, *2*, 13. [CrossRef]